CANCER

Fast label-free multilayered histology-like imaging of human breast cancer by photoacoustic microscopy

Terence T. W. Wong,[1] Ruiying Zhang,[1] Pengfei Hai,[1] Chi Zhang,[1] Miguel A. Pleitez,[1] Rebecca L. Aft,[2,3]* Deborah V. Novack,[4,5]* Lihong V. Wang[1]*†

The goal of breast-conserving surgery is to completely remove all of the cancer. Currently, no intraoperative tools can microscopically analyze the entire lumpectomy specimen, which results in 20 to 60% of patients undergoing second surgeries to achieve clear margins. To address this critical need, we have laid the foundation for the development of a device that could allow accurate intraoperative margin assessment. We demonstrate that by taking advantage of the intrinsic optical contrast of breast tissue, photoacoustic microscopy (PAM) can achieve multilayered histology-like imaging of the tissue surface. The high correlation of the PAM images to the conventional histologic images allows rapid computations of diagnostic features such as nuclear size and packing density, potentially identifying small clusters of cancer cells. Because PAM does not require tissue processing or staining, it can be performed promptly and intraoperatively, enabling immediate directed re-excision and reducing the number of second surgeries.

INTRODUCTION

In 2015, an estimated ~300,000 new cases of invasive and noninvasive breast cancer were diagnosed in U.S. women (1). Of these, 60 to 75% were treated with breast-conserving surgery (BCS) as the initial therapy. The goal of BCS is to excise the tumor with a rim of normal surrounding tissue so that no cancer cells remain at the cut margin (fig. S1A, negative margin) while preserving as much normal breast tissue as possible. The current standard is to find no tumor at the edge of the specimen via histologic analysis (2) because negative margins reduce the local recurrence rate (3–5). Thus, those patients with cancer cells at the cut margin (fig. S1B, positive margin) most commonly require a second surgical procedure to obtain clear margins. Re-excision surgeries increase health care costs and the risk of complications, burden patients physically and psychologically, and potentially delay recommended adjuvant treatment. Several approaches have been used to decrease the positive margin rate to avoid re-excision (6, 7). However, these techniques may be ineffective in reducing the reoperative rate (8–12), difficult to master by surgeons (13), or time-consuming for large specimens (14, 15). As a result, despite the use of preoperative methods and intraoperative techniques, 20 to 60% of patients undergoing BCS require second surgeries due to positive surgical margins (16–24).

The standard of care for surgical margin assessment is postoperative examination of histopathological sections for cancer cells. Intraoperatively, histologic examination of tissue can be performed by frozen sectioning, which is limited by the difficulties of freezing adipose-rich tissue, typical of breast specimens, and the amount of time required to analyze large surface areas of tissue. For these reasons, frozen-section histology has not been widely incorporated into surgical practice for margin assessment during BCS. The ideal tool for margin assessment would have the same accuracy as histologic analysis without the need for processing specimens. To achieve this goal, we have developed and refined label-free photoacoustic (PA) tomography (PAT) for breast specimens. PAT requires minimal tissue handling, thus shortening specimen preparation and diagnosis. Label-free PA imaging with cellular resolution of surgical specimens could potentially provide fast and accurate breast tumor margin analysis at the time of the initial procedure, which would provide immediate feedback to surgeons for intraoperative decision-making.

PAT is a rapidly growing imaging modality that can provide volumetric images of biological tissue with scalable spatial resolutions and imaging depths (25, 26). PAT can be categorized into two primary imaging modes: PA microscopy (PAM) and PA computed tomography (PACT). In optical-resolution PAM mode, the imaging resolution is limited by the diffraction of light, and the imaging depth is governed by ballistic photons. Unlike other fluorescence- or scattering-based optical imaging modalities, PAT is based on optical absorption contrast, which, with appropriate wavelength illumination, is highly specific for a variety of targets (25, 26). Using multiwavelength illumination, different cellular and biological components can be imaged, such as cell nuclei (27), cytochromes (28), blood (29), melanin pigment (30), and lipid (31), all without the need for an exogenous contrast agent. Ultraviolet (UV) laser illumination has the advantage of highlighting cell nuclei, thus providing the same contrast as hematoxylin labeling used in conventional histology and measuring features related to the histologic landscape without the need for labels (27). Hence, together with an acoustically defined axial resolution, UV-PAM can provide multilayered histology-like imaging of the surface of breast tissue without physical sectioning, which is not achievable by bright-field optical imaging. Here, we developed and optimized a UV-PAM system to enable label-free, high-resolution, and specific imaging of fixed, unprocessed breast tissue.

RESULTS

Our UV-PAM system (Fig. 1), which can handle specimens of various thicknesses, produces images by detecting acoustic waves generated by laser-induced rapid thermoelastic expansion (25, 26). A focused ultrasonic transducer detects the one-dimensional (1D) depth-resolved PA signals (A-lines). Cross-sectional images (B-scans) or volumetric images (C-scans) can be produced by linear or raster scanning, respectively, using

[1]Optical Imaging Laboratory, Department of Biomedical Engineering, Washington University in St. Louis, St. Louis, MO 63130, USA. [2]Department of Surgery, Washington University School of Medicine, St. Louis, MO 63110, USA. [3]John Cochran Veterans Hospital, St. Louis, MO 63106, USA. [4]Musculoskeletal Research Center, Division of Bone and Mineral Diseases, Department of Medicine, Washington University School of Medicine, St. Louis, MO 63110, USA. [5]Department of Pathology, Washington University School of Medicine, St. Louis, MO 63110, USA.
*Corresponding author. Email: aftr@wudosis.wustl.edu (R.L.A.); novack@wustl.edu (D.V.N.); LVW@Caltech.edu (L.V.W.)
†Present address: Caltech Optical Imaging Laboratory, Andrew and Peggy Cherng Department of Medical Engineering, Department of Electrical Engineering, California Institute of Technology, 1200 East California Boulevard, MC 138-78, Pasadena, CA 91125, USA.
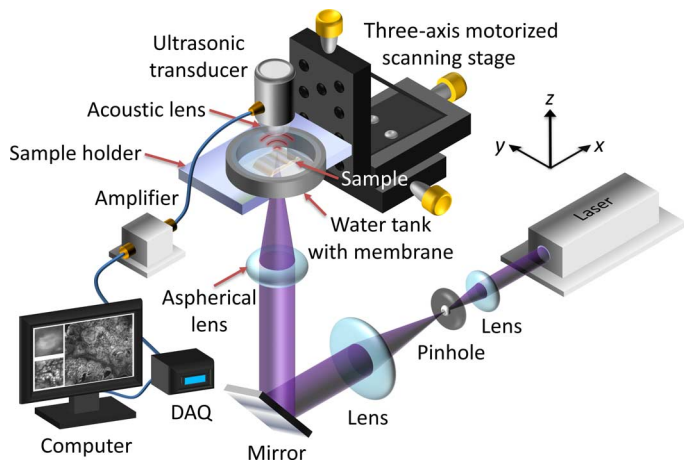
Fig. 1. Schematic of the UV-PAM system for surgical margin imaging. The UV laser beam is first spatially filtered and expanded by a pair of lenses and a pinhole. The beam is then focused through an aspherical lens onto the bottom of the breast tissue specimen (sample), which is placed inside a water tank on top of a sample holder. Some generated acoustic waves propagate through the tissue and reach a focused ultrasonic transducer. The received acoustic pressure is transduced into an electric signal, which is then amplified and recorded by a data acquisition (DAQ) card. During data acquisition, a maximum amplitude projection (MAP) image from the measured B-scan data is displayed on a computer screen within approximately 1 s. By raster-scanning the sample holder, a MAP image from the C-scan data is also displayed.

a motorized scanning stage. The UV-PAM system records and displays the PA B-scan images in real time during data acquisition. Because different absorbers intrinsically have different optical absorption spectra, when one absorber dominates at a chosen wavelength, a single-wavelength laser can be used to probe a specific biological component without resorting to exogenous labels. In cancer histology, the size variation and packing densities of cell nuclei can be used to identify cancer cell clusters (*32*). Therefore, UV light (266 nm), which DNA and RNA in cell nuclei absorb by an order of magnitude more strongly than other biological components (*27*), is used for illumination in our UV-PAM system. At this short wavelength, high spatial resolution can be achieved. The lateral imaging resolution was experimentally measured to be ~330 nm (fig. S2B), comparable to that of a conventional bright-field optical microscope with a high numerical aperture (NA) and sufficient to identify individual cell nuclei. Therefore, UV-PAM images should be able to reveal individual cell nuclear information without labeling.

Imaging of a section of breast tumor specimen without and with hematoxylin and eosin staining

To initially validate the performance of UV-PAM for breast tissue imaging, we imaged a section of the tissue cut from a formalin-fixed, paraffin-embedded block of breast tissue that had not been stained with hematoxylin and eosin (H&E) (fig. S3). We raster-scanned a thin slice over a 5 mm × 5 mm area along the *x* and *y* axes for ~100 min. Note that, in PAM, raster scanning generally produces a volumetric image. However, because the section slice was only 5 μm thick, which is finer than our axial resolution (fig. S2C), only 2D images are presented (Fig. 2). As a result of the intrinsic optical absorption, cell nuclei appear to be the brightest in UV-PAM images. After PA imaging, the slice was deparaffinized, H&E-stained, and imaged with optical microscopy. Comparison of the cell architecture between the UV-PAM image (Fig. 2A) and the H&E-stained image (Fig. 2B) reveals multiple similarities. Well-defined borders between normal tissue and tumor, which is mostly invasive

ductal carcinoma, are outlined with green dashed lines in the images (Fig. 2, A and B). The normal region (Fig. 2C, red dashed region) in the UV-PAM image (Fig. 2A) has a correlation coefficient of 0.74 with its corresponding position in the H&E-stained image (Fig. 2D). We overlaid the magnified H&E-stained image on its respective UV-PAM image to show their similarity (Fig. 2E). Similarly, the tumor region (Fig. 2F, yellow dashed region) in the UV-PAM images has a correlation coefficient of 0.64 with its H&E-stained image (Fig. 2G). The overlaid image is shown in Fig. 2H. The areas with imperfect spatial overlap were mainly due to structures that had been locally deformed during the subsequent sample preparation after PA imaging, which can be easily seen by comparing the features on the top right-hand corners of Fig. 2 (C and D), marked with blue dashed lines and arrows. We emphasize that although the correlation coefficients were diminished by local deformation, corresponding fundamental characteristics of the tissue structures are present in both UV-PAM and H&E-stained images. Purple, pink and red, and white in the H&E-stained images correspond to the brightest, moderately bright, and dark features, respectively, in the grayscale UV-PAM images. This color correspondence agrees well with the optical absorption-based contrast expectation. Purple labels the cell nuclei, which intrinsically absorb UV light most strongly. Pink and red indicate the cytoplasm, connective tissue, and other extracellular substances, which absorb UV light less strongly. White represents adipocytes, which appear as a void due to loss of lipid during tissue processing and appear dark in UV-PAM images because no absorbers were present to produce acoustic signals.

Label-free UV-PAM of fixed, unprocessed human breast tumors versus traditional microscopy of specimens processed with standard histology

To show the full potential of UV-PAM, we imaged formalin-fixed but unprocessed human breast tumors (Figs. 3 and 4 and fig. S4). After surgical excision, the breast tumors were fixed in formalin to prevent tissue degradation. Small samples were taken from the tumor/normal interface and sent for PA imaging. We emphasize that before PA imaging, the breast tumors were only fixed and did not undergo any further processing. Subsequently, the specimens were processed according to standard tissue preparation protocols (that is, paraffin embedding, sectioning, and H&E staining). Sections corresponding to the UV-PAM images were analyzed by conventional bright-field optical microscopy. Because the UV-PAM system images the surface and subsurface of a specimen (fig. S5), to prepare the best corresponding H&E-stained images, superficial sections were used. These H&E-stained sections did not exactly replicate the surface imaged by UV-PAM, but the image features are still markedly similar.

For the fixed, unprocessed breast tumor specimen from the first patient, the region of interest (ROI) was 10 mm × 4.2 mm (fig. S6A). Figure 3A shows a UV-PAM image of the ROI. The scanning time was ~180 min. The specimen was put in a laboratory-made sample holder, which flattened the tissue for wide field-of-view (FOV) in-focus imaging. A section was reimaged to show the image's reproducibility (fig. S7). Movie S1 shows a series of closeup UV-PAM images of a row of the ROI. Fundamental characteristics of the cancer structures, tumor margin, and normal tissue can all be identified in the closeup scanning UV-PAM images. Movie S2 shows a series of depth-resolved UV-PAM images of a portion of the ROI. Two closeup depth-resolved UV-PAM images of the cancer regions are also simultaneously shown to illustrate the strength of the multilayered imaging capability provided by UV-PAM over conventional histology. After PA imaging, the corresponding sections

were prepared histologically, and images were acquired (Fig. 3B). The closeup UV-PAM images (Fig. 3, C and E) reveal features similar to their corresponding H&E-stained images (Fig. 3, D and F). Each image centers on expanded breast ducts with a cribriform pattern of cellular proliferation, characteristic of ductal carcinoma in situ, that can be read-ily discerned in both the UV-PAM and H&E-stained images. Smaller nests of densely packed nuclei, representing invasive ductal carcinoma, can also be seen along the top edge in Fig. 3 (C to F). From another closeup UV-PAM image (Fig. 3G), it is clear that our imaging system is capable of imaging individual cell nuclei.
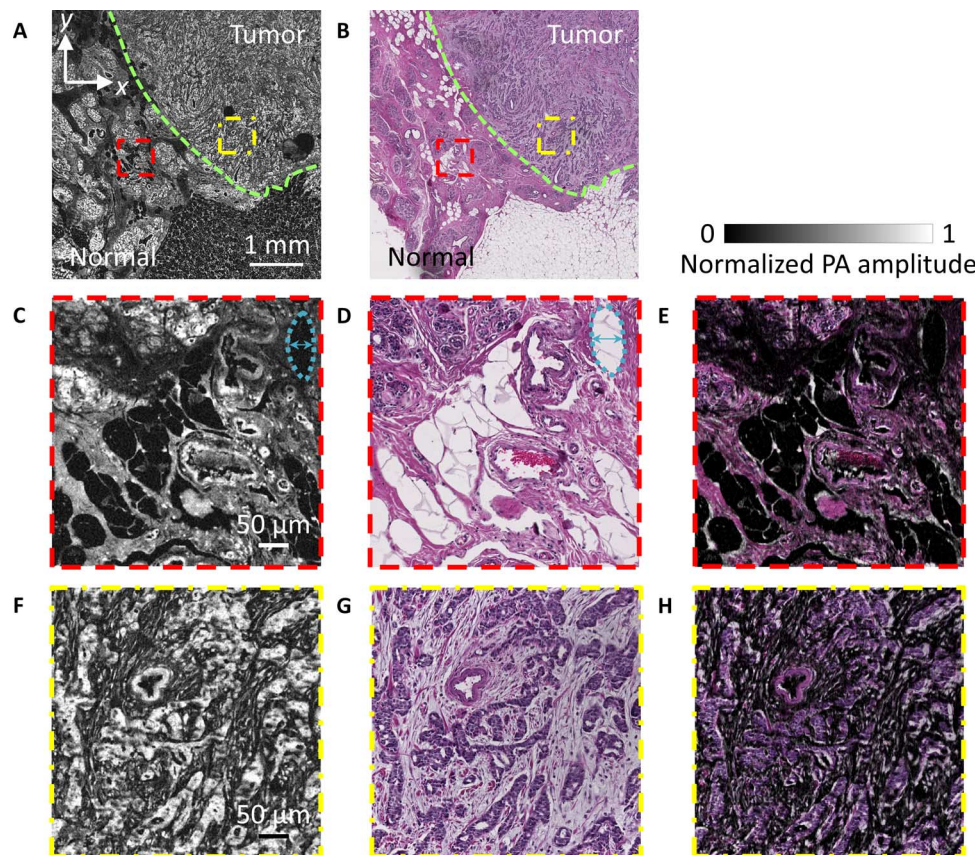

Fig. 2. Imaging of thin breast tissue slices without and with H&E staining. (**A**) Unstained paraffin-embedded breast tissue slice imaged by the UV-PAM system. (**B**) H&E-stained deparaffinized breast tissue slice imaged by a standard microscope. The green dashed lines in (A) and (B) outline the boundaries of the normal and tumor regions. The upper-right area is the tumor region, and the bottom-left area is the normal region. (**C** and **D**) Zoomed-in UV-PAM and H&E-stained images of the normal regions (red dashed regions) in (A) and (B), respectively. The blue dashed lines and arrows on the top right-hand corners in (C) and (D) label a representative local deformation. (**E**) Overlay image of (D) on (C). (**F** and **G**) Zoomed-in UV-PAM and H&E-stained images of the tumor regions (yellow dashed regions) in (A) and (B), respectively. (**H**) Overlay image of (G) on (F).
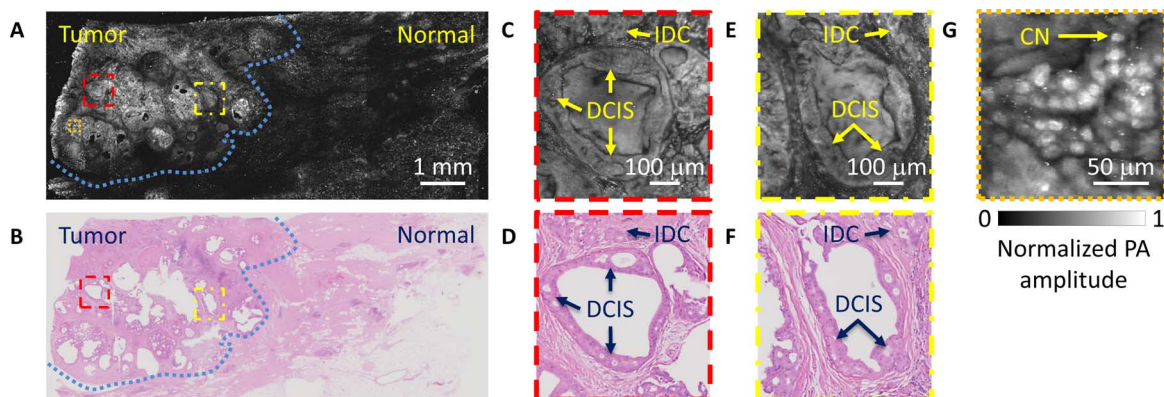

Fig. 3. Imaging of a breast tumor from the first patient. (**A**) UV-PAM image of the fixed, unprocessed breast tumor. (**B**) H&E-stained histologic image of the same area shown in (A) acquired after processing, sectioning, and staining the excised breast tissue. The blue dashed lines in (A) and (B) outline the interface between the normal and tumor regions. (**C** and **D**) Zoomed-in UV-PAM and H&E-stained images of the red dashed regions in (A) and (B), respectively. (**E** and **F**) Zoomed-in UV-PAM and H&E images of the yellow dashed regions in (A) and (B), respectively. IDC, invasive ductal carcinoma; DCIS, ductal carcinoma in situ. (**G**) Zoomed-in UV-PAM image of the orange dashed region in (A). CN, cell nuclei.
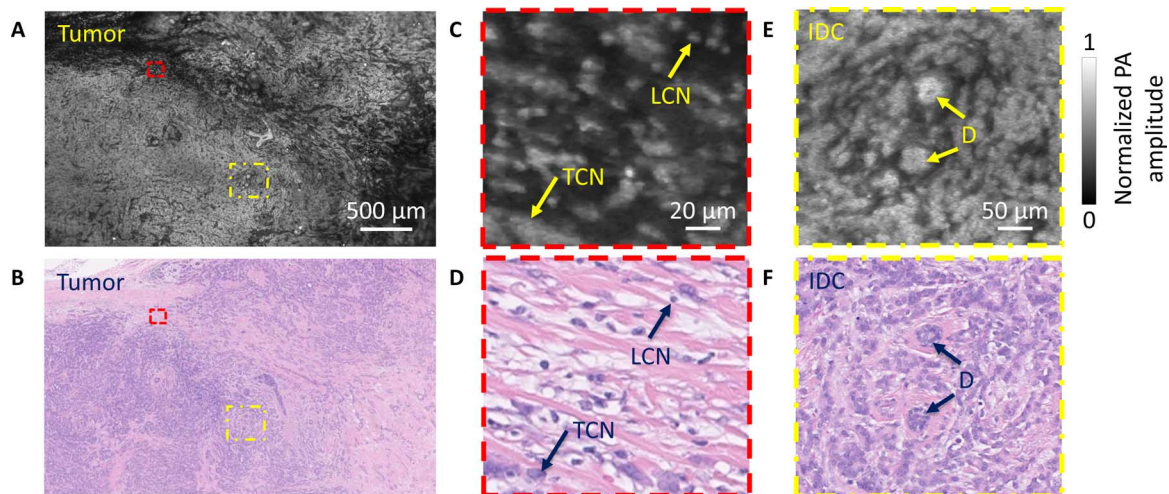
Fig. 4. Imaging of a breast tumor from the second patient. (**A**) UV-PAM image of the fixed, unprocessed breast tumor. (**B**) H&E-stained histologic image of the same area shown in (A) acquired after processing, sectioning, and staining the excised breast tissue. (**C** and **D**) Zoomed-in UV-PAM and H&E images of the red dashed regions in (A) and (B), respectively. LCN, lymphocyte cell nucleus; TCN, tumor cell nucleus. (**E** and **F**) Zoomed-in UV-PAM and H&E-stained images of the yellow dashed regions in (A) and (B), respectively. D, duct. The two ducts are surrounded by invasive ductal carcinoma.

For the second patient, an ROI of 7.5 mm × 4.5 mm (fig. S6B) was imaged by our UV-PAM system (Fig. 4A). The corresponding H&E-stained image is shown in Fig. 4B. The closeup UV-PAM image (Fig. 4C) shows a number of small bright cell nuclei that correspond to lymphocytes on the histologic image (Fig. 4D). Lymphocytes are often associated with cancer. Comparing the two closeup images (Fig. 4, C and D), we observe denser lymphocytes in our UV-PAM image. This difference can be explained by the greater imaging penetration depth of UV-PAM (fig. S5) compared to the sectioned slice thickness of the H&E-stained tissue.

When the cell nuclei are densely packed along the lateral and axial directions, individual cell nuclei cannot be resolved, resulting in a bright and dense feature, as seen in another closeup UV-PAM image (Fig. 4E). In this case, the corresponding H&E-stained image (Fig. 4F) demonstrates densely packed breast tumor cells. For a third patient sample, the ROI was 7.8 mm × 3 mm (fig. S6C). As with the second patient, in our UV-PAM image, we can see a bright signal in the left region (fig. S4A). This region also represents a high-grade tumor, as shown in the corresponding H&E-stained image (fig. S4B). This H&E-stained image reveals relatively large empty regions, which are fully filled in the UV-PAM image, due to the rough surface of the third specimen. Therefore, these UV-PAM and H&E-stained images (fig. S4, A and B) clearly show that the greater imaging depth allows the UV-PAM system to provide more cellular structural information than a corresponding H&E-stained thin section of the same tissue.

To show that diagnostic features can be computed quantitatively from our UV-PAM images, we measured the sizes and the internuclear distances of the cell nuclei from various cell types in both UV-PAM and H&E-stained images. In particular, nuclear features from breast cancer cells were derived from Fig. 3 (C and D), whereas lymphocyte nuclear features were derived from Fig. 4 (C and D). Our results show that the calculated distribution of the nuclear area per cell values from UV-PAM images is similar to that from H&E-stained images (Fig. 5, A and B) in terms of mean values and standard deviations (SD). On the basis of the nuclear cross-sectional area, breast cancer cells and lymphocytes can be readily distinguished (Fig. 5, A and B). Our results also show that the calculated distributions of the internuclear distances of breast cancer cells

and lymphocytes from the UV-PAM images are similar to those from the H&E-stained images (Fig. 5, C and D) with good agreement in mean and SD values. These results further support the accuracy of the information that can be extracted from UV-PAM images, which would potentially enable accurate PAM-based histologic assessment of cancer specimens.

DISCUSSION
Implementation of an intraoperative UV-PAM system for breast tumor excision could be transformative. Our UV-PAM system was able to image fixed, unprocessed breast tumors with an image quality comparable to that of conventional histology using processed, paraffin-embedded, sectioned, and H&E-stained specimens (Figs. 3 and 4 and fig. S4). Although fixed breast tumors were imaged in this study to maintain tissue integrity during relatively long intervals between surgery and processing for histology, fresh breast tumors are expected to provide similar imaging contrast (33). With relevant information regarding such tissue features as the average nuclear size and internuclear distance (Fig. 5), typically obtained from histology, UV-PAM images could be used to detect cancer cell clusters at the margins of tissue specimens during a surgical procedure, allowing immediate action to achieve clear margins. Although benign breast epithelial cells are too few in the UV-PAM images to be compared with cancer cells, the close correspondence between UV-PAM and histology for both lymphocytes and cancer cells provides the proof of concept that UV-PAM can be used to examine diagnostically relevant parameters.

To fulfill the clinical needs of an intraoperative assessment, imaging throughput has to be improved. Currently, acquiring an approximately 1 cm × 1 cm image with a spatial resolution comparable to that of a traditional high-NA optical microscope takes about 7 hours. However, multichannel parallel imaging can shorten the scanning time by orders of magnitude. For instance, the laser beam can be focused to more than 80 × 80 spots by a microlens array while the generated PA waves are received by an ultrasonic transducer array simultaneously (34). For intraoperative margin analysis of surgical specimens, it would be ideal to scan the entire surface of a specimen, although the current gold standard histology is to spot-check only selected regions owing to
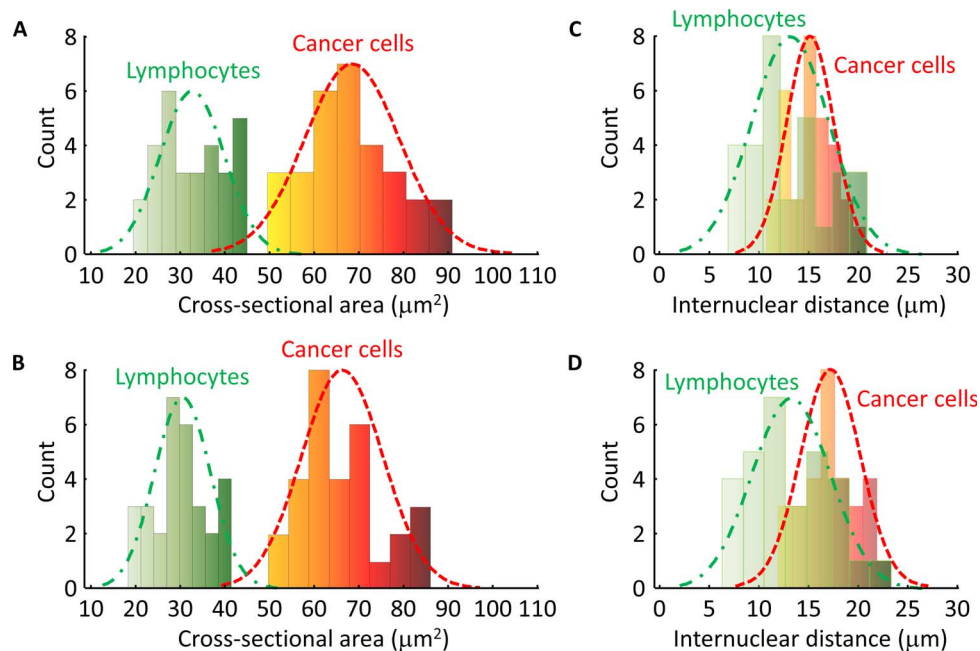
Fig. 5. Distributions of cell nuclear area values and internuclear distances in the breast tumor specimens (Figs. 3 and 4), where bin interval = 8 and n = 30 for each distribution. (**A**) Histogram of the cell nuclear cross-sectional areas imaged by UV-PAM (Figs. 3C and 4C). The green dashed line is a Gaussian fit for lymphocytes, with a mean of 32.8 μm^2 and an SD of 7 μm^2. The red dashed line is a Gaussian fit for cancer cells, with a mean of 67.6 μm^2 and an SD of 11 μm^2. (**B**) Histogram of the cell nuclear cross-sectional areas imaged by histology (Figs. 3D and 4D). The green dashed line is a Gaussian fit for lymphocytes, with a mean of 30.1 μm^2 and an SD of 6.7 μm^2. The red dashed line is a Gaussian fit for cancer cells, with a mean of 66 μm^2 and an SD of 9.2 μm^2. (**C**) Histogram of the internuclear distances imaged by UV-PAM (Figs. 3C and 4C). The green dashed line is a Gaussian fit for lymphocytes, with a mean of 13.1 μm and an SD of 3.8 μm. The red dashed line is a Gaussian fit for cancer cells, with a mean of 15.4 μm and an SD of 2.4 μm. (**D**) Histogram of the internuclear distances imaged by histology (Figs. 3D and 4D). The green dashed line is a Gaussian fit for lymphocytes, with a mean of 13.2 μm and an SD of 4.1 μm. The red dashed line is a Gaussian fit for cancer cells, with a mean of 17.2 μm and an SD of 2.9 μm.

limited throughput. Because a typical breast lumpectomy specimen has a diameter of less than 5 cm with a thickness of ~1 cm, the total surface area is less than ~55 cm^2, which could be imaged within 4 min. With this imaging duration combined with computer-aided detection (35), feedback could be provided intraoperatively to surgeons.

The functionality of the UV-PAM system can be boosted in two ways. First, instead of imaging excised, fixed, and unprocessed breast tissue using a benchtop UV-PAM system, it is possible to design the UV-PAM system in a handheld probe configuration that allows in vivo imaging of breast tissue. With a high–repetition rate laser, real-time UV-PAM images can be provided with an imaging FOV of ~3 mm × 3 mm. This capability would enable "virtual" histology-guided BCS, which would allow surgeons to see histology-like images of remaining breast tissue after tumor excision and allow immediate detection and removal of residual tumor. UV light in vivo can be safely used at the targeted imaging depth of ~100 μm because the corresponding surface's laser exposure is <0.1 mJ/cm^2 for the current UV-PAM images and thus well within the American National Standards Institute safety standard, which sets the maximum permissible exposure at 3 mJ/cm^2 for this wavelength (33). Second, the imaging specificity of the UV-PAM system can be improved by using a multiwavelength technique. Although UV illumination can probe cell nuclei, other breast tissue structures, such as stroma and microcalcification, absorb UV light at lower but still similar levels and appear moderately bright with comparable signal amplitudes in the UV-PAM images. With hydroxyapatite absorption contrast, using a 700-nm laser would allow the identification of microcalcifications (36), which are associated with some breast cancers (37, 38).

One limitation of the UV-PAM imaging performed here is that densely packed cell nuclei create a bright signal (Fig. 4, A, B, E, and F, and fig. S4, A and B), preventing the observation of individual cell nuclei. This effect is likely due to the difference in imaged thicknesses (~100 μm in UV-PAM versus ~5 μm in H&E). The intense signal could lead to false-positive margin calls when dense lymphocytes rather than tumor cells generate this pattern. Equipping the UV-PAM system with optical sectioning capability, which can be achieved by several different approaches, such as Gruneisen relaxation (39), would improve the axial resolution. With optical sectioning, UV-PAM could image a thickness of breast tissue equivalent to standard histologic sections, likely eliminating this confounding imaging pattern. Furthermore, with improved axial resolution, it is possible to reconstruct a detailed volumetric image of breast tumor specimens with more resolvable points along the axial direction, enabling 3D information extraction. This previously inaccessible information could potentially boost the accuracy of specimen analysis.

In summary, we have developed and optimized UV-PAM of breast tissues, generating images of cellular structures and organizations similar to that seen on histologic sections stained with H&E. Diagnostic features, such as the sizes and internuclear distances of cell nuclei, can be computed accurately from our UV-PAM images. These features have been found to relate to cytologic and histologic grade, tumor size, nodal status, and clinical stage (40). With these useful parameters, automatic algorithms could be developed to recognize malignancy in UV-PAM images. We believe that this is the first step toward the development of an intraoperative margin assessment tool that can be used by surgeons and pathologists to detect and distinguish cancer cells and normal

cells at surgical margins. Although we have concentrated on breast tissue, we believe that UV-PAM can be optimized for other cancer specimens where margin status is critical for patient outcome, such as pancreatic cancer and glioblastoma.

MATERIALS AND METHODS

Human breast tissue ex vivo imaging experiments

After informed consent was obtained, breast cancer specimens were collected from women with newly diagnosed stage I/II breast cancer undergoing BCS. The protocol was approved by the Institutional Review Board at Washington University in St. Louis. After excision, breast tumor specimens were placed in formalin and sectioned through the tumor under the supervision of a pathologist (D.V.N.). One-half of the specimen was used for histologic analysis, and the other half was used for PAM imaging.

Transmission-mode UV-PAM system

Our transmission-mode UV-PAM system (Fig. 1) used light at 266 nm, which is emitted by a Nd:YLF (neodymium-doped yttrium lithium fluoride) Q-switched UV laser (QL266-010-O, CrystaLaser Inc.). The laser beam was expanded 50 times by a pair of lenses (LA4647-UV and LA4663-UV, Thorlabs Inc.) and spatially filtered by a 25-μm-diameter pinhole (#59-255, Edmund Optics Inc.). The beam was subsequently focused by an aspherical lens (A25-25FPX-S-X, asphericon GmbH) to illuminate the specimen from below. The specimen was sandwiched between a laboratory-made water tank with a membrane, which was placed on the sample holder, and a quartz slide/coverslip. The gap between the membrane and the specimen was filled with water to ensure effective acoustic coupling. The PA waves were generated at the bottom surface of the specimen. Finally, the upward propagating PA waves were focused by a laboratory-made acoustic lens and detected by a water-immersed ultrasonic transducer (V214-BB-RM, Olympus NDT Inc.) with a central frequency of 50 MHz. The working distance of the ultrasonic transducer is ~6 mm.

Lateral and axial resolution measurements by gold nanoparticles

The lateral and axial resolutions of the UV-PAM system were measured by imaging 50-nm-diameter gold nanoparticles (fig. S2A). Five gold nanoparticles were segmented and averaged to provide data points for Gaussian profile fitting to measure the lateral resolution. The full width at half maximum (FWHM) of the Gaussian fit profile is ~330 nm (fig. S2B), which is close to the theoretical value of ~280 nm for the 0.48 NA of the aspherical lens. To measure the axial resolution, we used the A-line signal of the gold nanoparticle's center position (fig. S2A). The FWHM of the amplitude of the Hilbert-transformed A-line signal reveals the axial resolution of the imaging system. It measures ~32.5 ns (fig. S2C), which corresponds to ~48 μm for a speed of sound of ~1480 m/s. The theoretical value is calculated to be ~42 μm, which is similar to the experimental value. With the current penetration depth for breast tissues (fig. S5), there are about three resolvable voxels in the axial dimension. Hence, depth-resolved images can be achieved (movie S2).

UV-PAM of fixed, paraffin-embedded breast tumor specimen versus conventional microscopy of specimen processed with standard histology

The procedure for preparing thin breast tissue slices without and with H&E staining is shown in fig. S3. For UV-PAM imaging, a quartz slide,

which is a UV transparent material, was used instead of a glass slide below the sectioned breast tumor. This material ensured effective light delivery to the breast tissue. The quartz slide was put on the sample holder, and the tissue was covered by a water tank with a membrane window. Note that no coverslip was used, and water was added between the tissue-to-membrane interfaces to ensure effective acoustic coupling. Last, the water tank was filled with water, and the focused ultrasonic transducer was immersed for acoustic wave detection. After PA imaging, the tissue slice was sent back to the pathologist for H&E staining and corresponding histologic imaging.

UV-PAM of fixed, unprocessed breast tumor specimens versus conventional microscopy of specimens processed with standard histology

Preparation of all breast tumor specimens followed the same protocol. The specimens were promptly delivered from the pathologist to the PA imaging laboratory. During delivery, the specimen was immersed in 10% neutral buffered formalin (NBF) to maintain its rigidity and shape. Upon arrival, the breast tumor was put on a quartz coverslip, which served both as a flat platform for the rough breast tissue surface and as a transparent optical window for UV light illumination. When the specimen was further sandwiched by the water tank membrane, the breast tissue, which is ragged at the edges, was stretched over the quartz coverslip surface. This imaging platform design enabled wide-FOV in-focus imaging. As before, the water tank was put on the sample holder and filled with water for acoustic coupling. The acoustic waves generated were detected by the immersed ultrasonic transducer. After PA imaging, the thick breast tissue was put back into the NBF and returned to the pathologist. The breast tissue then underwent standard histology procedures for H&E staining. To make full FOV comparison with UV-PAM images, the H&E-stained slide was imaged with bright-field microscopy (NanoZoomer, Hamamatsu Photonics K.K.).

Data acquisition and processing

We developed a LabVIEW software–based data acquisition program. After acquiring all the user inputs, the computer transferred all the parameters to a central controller (sbRIO-9623, National Instruments Corp.), which integrated with a reconfigurable field-programmable gate array. The controller triggered the UV laser and the data acquisition card (ATS9350, Alazar Technologies Inc.) installed in the computer, and data were recorded on the computer hard disk, with real-time display on the computer screen. The controller also triggered the x and y scanning stages (PLS-85, PI miCos GmbH) in synchronization with the laser for point-by-point scanning of the specimen surface. Each laser pulse generated a 1D PA image (A-line) by recording the time course of the PA signal. Volumetric image of the specific optical absorption (J/m^3) of the specimen can be obtained by raster-scanning a motorized stage.

Calculations of the cell nuclear cross-sectional area and internuclear distance

Because cell nuclei have higher optical absorption than other tissue components at the illumination wavelength, they generated stronger PA signals. To distinguish cell nuclei from background, we set a contrast-to-noise ratio threshold of 6 dB, where noise was defined as the SD of the background area's amplitude. On the basis of the threshold, the PA image was then converted into a binary image. The cell nuclei were identified (that is, segmented) on the basis of the binary PA image. Because the lateral resolution of UV-PAM (0.33 μm) was much finer than the axial resolution (48 μm), the cell nuclear cross-sectional area was calculated in the lateral

plane. After the cell nuclei were identified, the center positions of the cell nuclei were located and used to compute the shortest adjacent distance to a neighboring cell nucleus to represent the internuclear distance.

SUPPLEMENTARY MATERIALS

Supplementary material for this article is available at http://advances.sciencemag.org/cgi/content/full/3/5/e1602168/DC1

fig. S1. Illustrations of negative and positive margins.
fig. S2. Experimentally measured spatial and axial resolutions of the UV-PAM system.
fig. S3. Procedure for obtaining thin breast tissue slices without and with H&E staining.
fig. S4. Imaging of a breast tumor from the third patient.
fig. S5. Representative xz-projected human breast tumor image acquired over a 10 mm × 4.2 mm area from the first patient specimen.
fig. S6. Photographs of the breast tissue specimens.
fig. S7. Reproducibility of the UV-PAM system for breast tumor tissue imaging.
movie S1. Closeup images of a row in the ROI of the first patient's breast tumor specimen imaged by UV-PAM.
movie S2. Series of depth-resolved images of the first patient's breast tumor specimen imaged by UV-PAM.

REFERENCES AND NOTES

1. American Cancer Society, "Breast Cancer Facts & Figures 2015–2016" (American Cancer Society Inc., 2015).
2. M. S. Moran, S. J. Schnitt, A. E. Giuliano, J. R. Harris, S. A. Khan, J. Horton, S. Klimberg, M. Chavez-MacGregor, G. Freedman, N. Houssami, P. L. Johnson, M. Morrow, Society of Surgical Oncology–American Society for Radiation Oncology consensus guideline on margins for breast-conserving surgery with whole-breast irradiation in stages I and II invasive breast cancer. *J. Clin. Oncol.* **88**, 553–564 (2014).
3. J. A. van Dongen, A. C. Voogd, I. S. Fentiman, C. Legrand, R. J. Sylvester, D. Tong, E. van der Schueren, P. A. Helle, K. van Zijl, H. Bartelink, Long-term results of a randomized trial comparing breast-conserving therapy with mastectomy: European Organization for Research and Treatment of Cancer 10801 trial. *J. Natl. Cancer Inst.* **92**, 1143–1150 (2000).
4. C. C. Park, M. Mitsumori, A. Nixon, A. Recht, J. Connolly, R. Gelman, B. Silver, S. Hetelekidis, A. Abner, J. R. Harris, S. J. Schnitt, Outcome at 8 years after breast-conserving surgery and radiation therapy for invasive breast cancer: Influence of margin status and systemic therapy on local recurrence. *J. Clin. Oncol.* **18**, 1668–1675 (2000).
5. C. Kunos, L. Latson, B. Overmoyer, P. Silverman, R. Shenk, T. Kinsella, J. Lyons, Breast conservation surgery achieving ≥ 2 mm tumor-free margins results in decreased local-regional recurrence rates. *Breast J.* **12**, 28–36 (2006).
6. R. G. Pleijhuis, M. Graafland, J. de Vries, J. Bart, J. S. de Jong, G. M. van Dam, Obtaining adequate surgical margins in breast-conserving therapy for patients with early-stage breast cancer: Current modalities and future directions. *Ann. Surg. Oncol.* **16**, 2717–2730 (2009).
7. A. B. Chagpar, B. K. Killelea, T. N. Tsangaris, M. Butler, K. Stavris, F. Li, X. Yao, V. Bossuyt, M. Harigopal, D. R. Lannin, L. Pusztai, N. R. Horowitz, A randomized, controlled trial of cavity shave margins in breast cancer. *N. Engl. J. Med.* **373**, 503–510 (2015).
8. N. H. Peters, S. Esser, M. A. van den Bosch, R. K. Storm, P. W. Plaisier, T. van Dalen, S. C. Diepstraten, T. Weits, P. J. Westenend, G. Stapper, M. A. Fernandez-Gallardo, I. H. Borel Rinkes, R. van Hillegersberg, W. P. Mali, P. H. Peeters, Preoperative MRI and surgical management in patients with nonpalpable breast cancer: The MONET—Randomised controlled trial. *Eur. J. Cancer* **47**, 879–886 (2011).
9. L. Turnbull, S. Brown, I. Harvey, C. Olivier, P. Drew, V. Napp, A. Hanby, J. Brown, Comparative effectiveness of MRI in breast cancer (COMICE) trial: A randomised controlled trial. *Lancet* **375**, 563–571 (2010).
10. T. M. Allweis, Z. Kaufman, S. Lelcuk, I. Pappo, T. Karni, S. Schneebaum, R. Spector, A. Schindel, D. Hershko, M. Zilberman, J. Sayfan, Y. Berlin, A. Hadary, O. Olsha, H. Paran, M. Gutman, M. Carmon, A prospective, randomized, controlled, multicenter study of a real-time, intraoperative probe for positive margin detection in breast-conserving surgery. *Am. J. Surg.* **196**, 483–489 (2008).
11. T. Karni, I. Pappo, J. Sandbank, O. Lavon, V. Kent, R. Spector, S. Morgenstern, S. Lelcuk, A device for real-time, intraoperative margin assessment in breast-conservation surgery. *Am. J. Surg.* **194**, 467–473 (2007).
12. S. B. Coopey, J. M. Buckley, B. L. Smith, K. S. Hughes, M. A. Gadd, M. C. Specht, Lumpectomy cavity shaved margins do not impact re-excision rates in breast cancer patients. *Ann. Surg. Oncol.* **18**, 3036–3040 (2011).
13. N. M. A. Krekel, M. H. Haloua, A. M. F. Lopes Cardozo, R. H. de Wit, A. M. Bosch, L. M. de Widt-Levert, S. Muller, H. van der Veen, E. Bergers, E. S. M. de Lange de Klerk, S. Meijer, M. P. van den Tol, Intraoperative ultrasound guidance for palpable breast cancer excision (COBALT trial): A multicentre, randomised controlled trial. *Lancet Oncol.* **14**, 48–54 (2013).
14. E. K. Valdes, S. K. Boolbol, J.-M. Cohen, S. M. Feldman, Intra-operative touch preparation cytology; does it have a role in re-excision lumpectomy? *Ann. Surg. Oncol.* **14**, 1045–1050 (2007).
15. S. E. Singletary, Surgical margins in patients with early-stage breast cancer treated with breast conservation therapy. *Am. J. Surg.* **184**, 383–393 (2002).
16. L. E. McCahill, R. M. Single, E. J. Aiello Bowles, H. S. Feigelson, T. A. James, T. Barney, J. M. Engel, A. A. Onitilo, Variability in reexcision following breast conservation surgery. *JAMA* **307**, 467–475 (2012).
17. M. Clarke, R. Collins, S. Darby, C. Davies, P. Elphinstone, V. Evans, J. Godwin, R. Gray, C. Hicks, S. James, E. MacKinnon, P. McGale, T. McHugh, R. Peto, C. Taylor, Y. Wang; Early Breast Cancer Trialists' Collaborative Group (EBCTCG), Effects of radiotherapy and of differences in the extent of surgery for early breast cancer on local recurrence and 15-year survival: An overview of the randomised trials. *Lancet* **366**, 2087–2106 (2005).
18. R. Jeevan, D. A. Cromwell, M. Trivella, G. Lawrence, O. Kearins, J. Pereira, C. Sheppard, C. M. Caddy, J. H. P. van der Meulen, Reoperation rates after breast conserving surgery for breast cancer among women in England: Retrospective study of hospital episode statistics. *BMJ* **345**, e4505 (2012).
19. L. Jacobs, Positive margins: The challenge continues for breast surgeons. *Ann. Surg. Oncol.* **15**, 1271–1272 (2008).
20. M. C. Lee, K. Rogers, K. Griffith, K. A. Diehl, T. M. Breslin, V. M. Cimmino, A. E. Chang, L. A. Newman, M. S. Sabel, Determinants of breast conservation rates: Reasons for mastectomy at a comprehensive cancer center. *Breast J.* **15**, 34–40 (2009).
21. W. Jung, E. Kang, S. M. Kim, D. Kim, Y. Hwang, Y. Sun, C. K. Yom, S.-W. Kim, Factors associated with re-excision after breast-conserving surgery for early-stage breast cancer. *J. Breast Cancer* **15**, 412–419 (2012).
22. G. C. Balch, S. K. Mithani, J. F. Simpson, M. C. Kelley, Accuracy of intraoperative gross examination of surgical margin status in women undergoing partial mastectomy for breast malignancy. *Am. Surg.* **71**, 22–28 (2005).
23. T. L. Huston, R. Pigalarga, M. P. Osborne, E. Tousimis, The influence of additional surgical margins on the total specimen volume excised and the reoperative rate after breast-conserving surgery. *Am. J. Surg.* **192**, 509–512 (2006).
24. A. Kobbermann, A. Unzeitig, X.-J. Xie, J. Yan, D. Euhus, Y. Peng, V. Sarode, A. Moldrem, A. M. Leitch, V. Andrews, C. Stallings, R. Rao, Impact of routine cavity shave margins on breast cancer re-excision rates. *Ann. Surg. Oncol.* **18**, 1349–1355 (2011).
25. L. V. Wang, S. Hu, Photoacoustic tomography: In vivo imaging from organelles to organs. *Science* **335**, 1458–1462 (2012).
26. L. V. Wang, Multiscale photoacoustic microscopy and computed tomography. *Nat. Photonics* **3**, 503–509 (2009).
27. D.-K. Yao, K. Maslov, K. K. Shung, Q. Zhou, L. V. Wang, In vivo label-free photoacoustic microscopy of cell nuclei by excitation of DNA and RNA. *Opt. Lett.* **35**, 4139–4141 (2010).
28. C. Zhang, Y. S. Zhang, D.-K. Yao, Y. Xia, L. V. Wang, Label-free photoacoustic microscopy of cytochromes. *J. Biomed. Opt.* **18**, 020504 (2013).
29. J. Yao, L. Wang, J.-M. Yang, K. I. Maslov, T. T. W. Wong, L. Li, C.-H. Huang, J. Zou, L. V. Wang, High-speed label-free functional photoacoustic microscopy of mouse brain in action. *Nat. Methods* **12**, 407–410 (2015).
30. H. F. Zhang, K. Maslov, G. Stoica, L. V. Wang, Functional photoacoustic microscopy for high-resolution and noninvasive in vivo imaging. *Nat. Biotechnol.* **24**, 848–851 (2006).
31. T. J. Allen, A. Hall, A. P. Dhillon, J. S. Owen, P. C. Beard, Spectroscopic photoacoustic imaging of lipid-rich plaques in the human aorta in the 740 to 1400 nm wavelength range. *J. Biomed. Opt.* **17**, 061209 (2012).
32. D. Zink, A. H. Fische, J. A. Nickerson, Nuclear structure in cancer cells. *Nat. Rev. Cancer* **4**, 677–687 (2004).
33. D.-K. Yao, R. Chen, K. Maslov, Q. Zhou, L. V. Wang, Optimal ultraviolet wavelength for in vivo photoacoustic imaging of cell nuclei. *J. Biomed. Opt.* **17**, 056004 (2012).
34. J. Xia, G. Li, L. Wang, M. Nasiriavanaki, K. Maslov, J. A. Engelbach, J. R. Garbow, L. V. Wang, Wide-field two-dimensional multifocal optical-resolution photoacoustic-computed microscopy. *Opt. Lett.* **38**, 5236–5239 (2013).
35. K.-H. Yu, C. Zhang, D. J. Berry, R. B. Altman, C. Ré, D. L. Rubin, M. Snyder, Predicting non-small cell lung cancer prognosis by fully automated microscopic pathology image features. *Nat. Commun.* **7**, 12474 (2016).
36. T.-C. Hsiao, Y.-Y. Cheng, W.-T. Tein, S.-B. Luo, D.-Y. Chiou, R.-J. Chung, M.-L. Li, Deep-penetration photoacoustic array imaging of calcifications. *J. Biomed. Opt.* **18**, 066002 (2013).
37. L. Liberman, A. F. Abramson, F. B. Squires, J. R. Glassman, E. A. Morris, D. D. Dershaw, The breast imaging reporting and data system: Positive predictive value of mammographic features and final assessment categories. *Am. J. Roentgenol.* **171**, 35–40 (1998).
38. R. Baker, K. D. Rogers, N. Shepherd, N. Stone, New relationships between breast microcalcifications and cancer. *Br. J. Cancer* **103**, 1034–1039 (2010).

39. L. Wang, C. Zhang, L. V. Wang, Grueneisen relaxation photoacoustic microscopy. *Phys. Rev. Lett.* **113**, 174301 (2014).

40. F. Abdalla, J. Boder, R. Markus, H. Hashmi, A. Buhmeida, Y. Collan, Correlation of nuclear morphometry of breast cancer in histological sections with clinicopathological features and prognosis. *Anticancer Res.* **29**, 1771–1776 (2009).